

Enhanced Current Transportation in Silicon-riched Nitride (SRN)/Silicon-riched Oxide (SRO) Multilayer Nanostructure

Yeliao Tao, Jun Zheng, Yuhua Zuo*, Chunlai Xue, Buwen Cheng, Qiming Wang

(Received 16 October; accepted 31 October; published online 10 November 2012.)

Abstract: A novel structure of silicon-riched nitride (SRN)/silicon-riched oxide (SRO) is proposed and prepared using RF reactive magnetron co-sputtering. High temperature annealing of SRN/SRO multilayers leads to formation of Si nanocrystals (NC) from isolating SRN and SRO layers simultaneously, which efficiently improves carrier transport ability compared to conventional SRN/Si₃N₄ counterpart. Micro-Raman scattering analysis reveals that SRN layer has dominating number of denser and smaller Si NCs, while SRO layer has relatively less, sparser and bigger Si NCs, as confirmed by high resolution transmission electron microscopy observation. The substitute SRO layers for Si₃N₄ counterparts significantly increase the amount of Si NCs as well as crystallization ratio in SRN layers; while the average Si NC size can be well controlled by the thickness of SRN layers and the content of N, and hence an obvious stronger absorption in UV region for the novel structure can be observed in absorption spectra. The *I-V* characteristics show that the current of hybrid SRN/SRO system increases up to 2 orders of magnitude at 1 V and even 5 orders of magnitude at 4 V compared to that of SRN/Si₃N₄ structure. Si NCs in SiO_y layers provide a transport pathway for adjacent Si NCs in SiN_x layers. The obvious advantage in carrier transportation suggests that SRN/SRO hybrid system could be a promising structure and platform to build Si nanostructured solar cells.

Keywords: Silicon nanostructure; Magnetron sputtering; Raman Spectroscopy; Charge transport

Citation: Yeliao Tao, Jun Zheng, Yuhua Zuo, Chunlai Xue, Buwen Cheng and Qiming Wang, "Enhanced Current Transportation in Silicon-riched Nitride (SRN)/Silicon-riched Oxide (SRO) Multilayer Nanostructure", Nano-Micro Lett. 4 (4), 202-207 (2012). <http://dx.doi.org/10.3786/nml.v4i4.p202-207>

Introduction

Silicon(Si) nanocrystals(NCs) embedded in dielectric matrix like SiO₂, Si₃N₄ or SiC have attracted interest vis-a-vis all-silicon tandem solar cells [1, 2] as well as silicon optoelectronics [3-7]. By utilizing the quantum confinement effect in Si NCs, an adjustable bandgap can be realized by controlling the NC sizes and hence the electron transfer among the Si NCs. Various deposition techniques have been used to fabricate Si NCs, which involve super-lattice, such as plasma-enhanced chemical vapor deposition (PECVD) [8], and co-sputtering [9]. The radio-frequency (RF) magnetron

sputtering technique for Si NC multilayer structure combined with post annealing is considered a cost-effective method [10,11].

In order to maximize the efficiency of solar cell, two processes need to be improved. Firstly, denser Si NCs in the multilayer can generate more electron-hole pairs during the absorption process. Secondly, increasing transport ability can extract more charge carriers via front and back contacts in the transport process. Lower bandgap barrier material like SiC instead of commonly used SiO₂ (Si₃N₄) [12, 13] or ultrathin barriers have been used to increase vertical carrier transport [14]. In this work, a novel structure of silicon-riched ni-

State Key Laboratory on Integrated Optoelectronics, Institute of Semiconductors, Chinese Academy of Sciences, Beijing 100083, China
*Corresponding author. Tel: 86-10-82304522. Fax: 86-10-82305052. E-mail: yhzuo@semi.ac.cn.

tride (SRN)/silicon-riched oxide (SRO) is proposed and prepared by RF reactive magnetron co-sputtering and post-annealing at 1100°C in N₂ atmosphere. SRO layer is introduced instead of traditional Si₃N₄ one. With Si NCs expected in otherwise isolation layer, the carrier transport may be improved. The morphology, absorption and transport properties of the novel SRN/SRO structure have been investigated in detail compared to the conventional SRN/Si₃N₄ counterpart.

Experimental

10 pairs of amorphous 3.5 nm SiN_y/3.5 nm SiO_x are deposited on both quartz and Si substrates by RF reactive magnetron co-sputtering using computer-controlled KJLC Lab 18 system. The base pressure is 1×10^{-7} Torr, and working gas pressure is 3 mTorr. The growth temperature is kept as 400°C. When growing SiN_y layer, the power density applied to Si target is 75 W, the gas flux ratio of N₂ to Ar is 4:100(SiN_x), 8:100(SiN_{x*}) or 16:100(Si₃N₄); while in growing SiO_x layer, the power density applied to Si and SiO₂ targets are 75 W and 30 W, alternatively. The post annealed procedure is conducted in N₂ atmosphere at 1100°C for 1 h. For comparison, 10 pairs of 3.5 nm SRO/3.5 nm SiO₂ and 3.5 nm SRN/3.5 nm Si₃N₄ stacks have been deposited and post-annealed under the same condition.

In order to study the morphology of the stacks, cross-sectional high-resolution transmission electron microscopy (HRTEM) observation was performed by a Tecnai G2 F20 S-Twin with incident electron energy of 200 kV. The TEM samples were prepared by standard mechanical and Ar ion thinning techniques. Micro-Raman scattering spectra were applied to investigate the microstructure of the films, using the 488 nm line of Ar ion laser and measured by JobinYvonHR800. For electrical characterization, circular Al electrodes with diameter of 1 mm were deposited on the front side of the samples, whereas the back surface of n⁺-Si substrates ($\rho = 0.001 \Omega\cdot\text{cm}$ - $0.005 \Omega\cdot\text{cm}$, $n = 0.8 \times 10^{20} \text{ cm}^{-3}$ - $1 \times 10^{20} \text{ cm}^{-3}$, thickness=400 μm) was entirely

covered with Al as the rear contact. The devices were annealed at 450°C for 0.5 h in N₂ atmosphere to improve the contact properties at the interface of Si NC layers/electrode. The current density as a function of the applied voltage was measured using a Suss PM8 probe station connected to an Agilent B1500A semiconductor parameter analyzer.

Results and discussion

HRTEM analysis

Figure 1 shows TEM micrographs of the annealed SiN_x/SiO_y sample. The total thickness of 75 nm is slightly larger as compared with the designed value of 70 nm. After thermal annealing, the periodic structure of the stack is not clear as shown in Fig. 1(a), due to the precipitation of excess Si nanocrystals (NCs) from both SiN_x and SiO_y layers. Figure 1(b) depicts a high-resolution TEM image of Si NCs. The lattice fringes correspond to isolated Si NCs, while the surrounding speckle pattern corresponds to amorphous SiO₂ or Si₃N₄. The average density of Si NCs is about $7 \times 10^{11} \text{ cm}^{-2}$. Most of Si NCs are well confined in each isolated SiN_x or SiO_y layers, and some larger Si NC penetrates both SiN_x and SiO_y layers, which will be discussed later. However, one should notice that the distribution of Si NC shows a very different behavior in different isolation layer. The density of Si NCs in SiN_x layers is larger than that in SiO_y layers, while the average size of Si NCs in SiN_x layer of 2.7 nm is smaller than that in SiO_y layers of 3.5 nm. That is, larger and sparser Si NC exists in SiO_y layer, while smaller and denser Si NC exists in SiN_x layer. The phenomena can be also observed in the following Micro-Raman analyzes. The origin will be discussed there.

Micro-Raman scattering spectra

Figure 2 shows Micro-Raman scattering spectra of all samples on quartz substrates, including standard c-Si substrate and as-deposited SiN_x/SiO_y sample. The

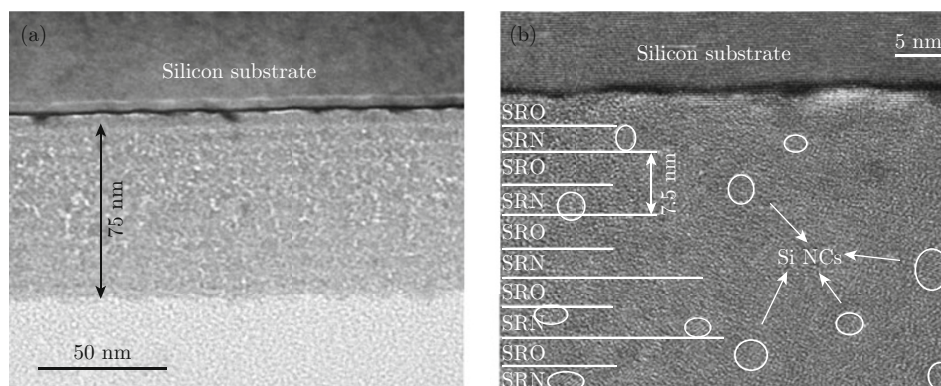


Fig. 1 TEM images of Si NCs of annealed SiN_x/SiO_y sample: (a) Low-magnification image and (b) High-resolution image.

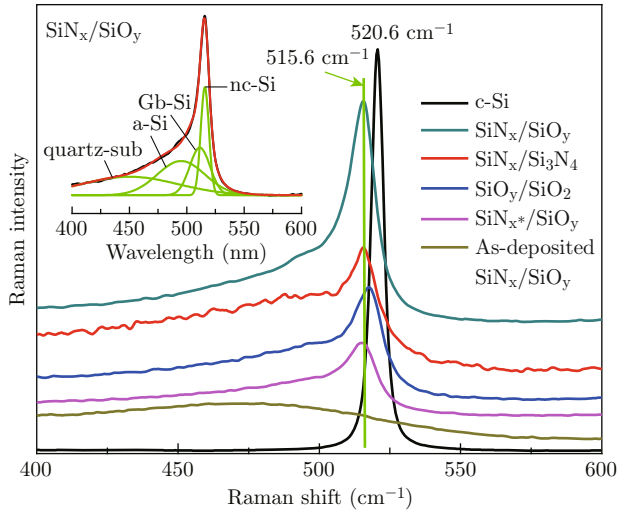


Fig. 2 Raman scattering spectra of all type of Si NCs structures and the Gaussian deconvoluted spectra of SiN_x/SiO_y structure.

as-deposited SiN_x/SiO_y film remains the amorphous phase characterized by the broadband peak centered at around 480 cm⁻¹ [15]; after annealing at 1100°C, a transition from amorphous to crystalline phase occurs through random nucleation of Si NC surrounded by *a*-Si, as indicated by the emergence of an intense peak with a frequency downshift compared to bulk Si Raman scattering spectra [16]. This frequency downshift may be caused by grain size related effect and compressive stress in the thin films [17,18]. Neglecting the stress effect, according to Zi's confinement model [19]: $\Delta\omega = \omega(D_z) - \omega_0 = -A(a/D_z)^\gamma$, where $\omega(D_z)$ is the frequency of the Raman phonon in a nanocrystal with size D_z , ω_0 (520.6 cm⁻¹) is the frequency of the optical phonon at the zone center for bulk crystal Si, and a is the lattice constant of Si (0.543 nm). The parameters A and γ , used to describe the vibration confinement due to the finite size in a nanocrystal, are 47.41 cm⁻¹ and 1.44, respectively. In this way, the sizes of Si NCs in four annealed samples can be obtained as summarized in Table 1.

Table 1 The list of analysis results of Raman scattering spectra

| Structure | Peak position (cm ⁻¹) | D (nm) | X_{gb} (%) | F_n (at.%) |
|--|-----------------------------------|----------|--------------|--------------|
| SiO _y /SiO ₂ | 517.7 | 3.28 | 26.6 | 46.3 |
| SiN _x /Si ₃ N ₄ | 515.6 | 2.58 | 24.6 | 36.2 |
| SiN _x /SiO _y | 515.6 | 2.58 | 26.5 | 50.9 |
| SiN _{x*} /SiO _y | 514.7 | 2.41 | 24.2 | 42.8 |

Besides the peak coming from quartz substrate, the Raman scattering spectra of annealed SiN_x/SiO_y can be well deconvoluted into three Gaussian components, as shown in the inset of Fig. 2. The first peak in the

region 460-490 cm⁻¹ comes from the TO vibrational modes of amorphous silicon. The second one, the intermediate component, arises near 505 cm⁻¹ associated with the bond dilation at grain boundaries. The third region at 515-517 cm⁻¹ is assigned to the TO mode of crystal grains of different sizes [18]. The crystalline and grain boundary volume fractions, F_n , and X_{gb} can be estimated from $F_n = (I_n + I_{gb}) / (\beta I_a + I_{gb} + I_n)$, $X_{gb} = I_{gb} / (\beta I_a + I_{gb} + I_n)$. Where I_a , I_{gb} and I_n are integrated intensities of the amorphous, intermediate and nanocrystalline peaks, respectively, and β represents the ratio of the cross section of the amorphous to crystalline phase, which varies with the grain size D , $\beta = 0.1 + \exp(-D/250)$ [20]. Using the D value calculated before, we obtain the crystalline volume fraction F_n listed in Table 1.

We notice that the average Si NCs size of SiN_x/SiO_y structure are the same as that of SiN_x/Si₃N₄ structure, with the value of 2.58 nm, while it is smaller than that in SiO_y/SiO₂ counterpart with the value of 3.28 nm. It means Si NCs in SiO_y layers have little impact on the average size of Si NCs in SiN_x/SiO_y structure, indicating that Si NCs are well confined in the isolated layers and the NC size in SiN_x layer dominates the average size since the number of NCs in SiN_x layer is much more than that in SiO_y layer. It can be concluded that the Si NCs in SiN_x layer is denser and smaller, while that in SiO_y layer is sparser and bigger. The result is consistent with the HRTEM observation.

Another important feature is that the crystalline volume fraction F_n of SiN_x/SiO_y structure, with the value of 50.9%, is obviously higher than 46.3% of SiO_y/SiO₂ structure and 36.2% of SiN_x/Si₃N₄ structure. Meanwhile, F_n decreases from 50.9% to 42.8%, along with the NC size reducing from 2.58 nm to 2.41 nm, when Si rich degree decreases with the concentration of nitrogen increasing from x to x^* . The higher F_n and more Si NCs in SiN_x layer may be explained by directional aggregation due to the distinguished difference of bond energy between Si-N (439 kJ/mol) and Si-O (799.6 kJ/mol). It was reported that nucleation of c-Si is suppressed near the Si/SiO₂ interface in the adjacent 0.5-1.0 nm of the Si layer [21]. However, during annealing procedure, the Si atoms near the SiN_x/SiO_y interfaces are in a trend to move to SiN_x layers to form a Si NC due to smaller Si-N bond energy, about only half of Si-O counterpart. Therefore, Si NCs can nucleate instead of being suppressed near the SiN_x/SiO_y interface, resulting in higher F_n . In some cases, one can expect large Si NC penetrates both layers, which can be confirmed by the HRTEM image in Fig. 1(b).

In conclusion, in SiN_x/SiO_y structure, compared to conventional SiO_y/SiO₂ and SiN_x/Si₃N₄ structure, the number of Si NCs in SiN_x increases significantly while that of Si NCs in SiO_y reduces and the total crystalline volume fraction is also improved. The SiN_x layer is the

dominating one, and both NC size and crystalline volume fraction of the novel $\text{SiN}_x/\text{SiO}_y$ structure can be well controlled by the thickness of SiN_x layer. Furthermore, the increasing number of Si NCs in SiN_x layers and existence of Si NCs in both SiN_x and SiO_y layers can substantially improve the transport properties which we will discuss later.

Optical properties

To clarify the impact of the substitute SRO layers for Si_3N_4 layers on optical properties, the optical bandgap energy of $\text{SiN}_x/\text{SiO}_y$, $\text{SiN}_x/\text{Si}_3\text{N}_4$ and $\text{SiN}_{x^*}/\text{SiO}_y$ samples is determined using Tauc's Equation [22], given as: $\alpha h\nu = B^{tauc} (h\nu - E_{gopt})^2$. Where α is the absorption coefficient, h is Plank's constant, and ν is the frequency of the radiation. B^{tauc} is the edge width parameter. α can be determined from the transmission and reflectance spectra, which is not shown here. Figure 3 shows the plot of $\alpha h\nu^{1/2}$ versus photon energy h of these samples. E_{gopt} evaluated from extrapolation of a linear part of the curve to intersect the energy axis ($\alpha h\nu = 0$). There is evidence that the absorption edge is all about 2.1 eV for these three samples which means the size of Si NCs is constant.

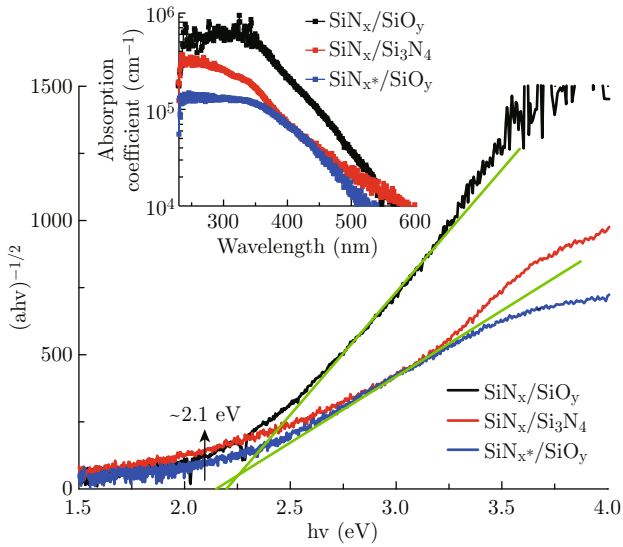


Fig. 3 Plot of $(\alpha h\nu)^{1/2}$ versus photon energy. The green lines are a fit of the Tauc curves. The inset illustrates the absorption coefficient of $\text{SiN}_x/\text{SiO}_y$, $\text{SiN}_x/\text{Si}_3\text{N}_4$ and $\text{SiN}_{x^*}/\text{SiO}_y$ samples.

The inset of Fig. 3 illustrates the absorption coefficient of $\text{SiN}_x/\text{SiO}_y$, $\text{SiN}_x/\text{Si}_3\text{N}_4$ and $\text{SiN}_{x^*}/\text{SiO}_y$ samples. The $\text{SiN}_x/\text{SiO}_y$ sample has an obvious stronger absorption in UV region due to more Si NCs in SiN_x layers. Compared with the $\text{SiN}_x/\text{Si}_3\text{N}_4$ and $\text{SiN}_{x^*}/\text{SiO}_y$ samples, the increased Si NCs can be explained by two reasons: (1) more Si atoms in SiN_x layers by controlling the Si/N ratio; (2) using SiO_y layer as a substitute for

Si_3N_4 layer. The absorption coefficient result is corresponding to the Raman spectra analysis.

Electrical characterization

Figure 4 shows the J - V characteristics of annealed $\text{SiN}_x/\text{Si}_3\text{N}_4$, $\text{SiN}_x/\text{SiO}_y$ and $\text{SiN}_{x^*}/\text{SiO}_y$ samples at room temperature. Hysteresis effect is not observed when the voltage is swept in forward direction and back to 0 V, which means the charging or electrically driven diffusion process of metal into films does not influence the J - V characteristics. As we expect, the hybrid $\text{SiN}_x/\text{SiO}_y$ system shows a huge increase up to 2 orders of magnitude at 1 V and even 5 orders of magnitude at 4 V compared to $\text{SiN}_x/\text{Si}_3\text{N}_4$ structure. The current decreases obviously when Si rich degree in SiN_x layer decreases.

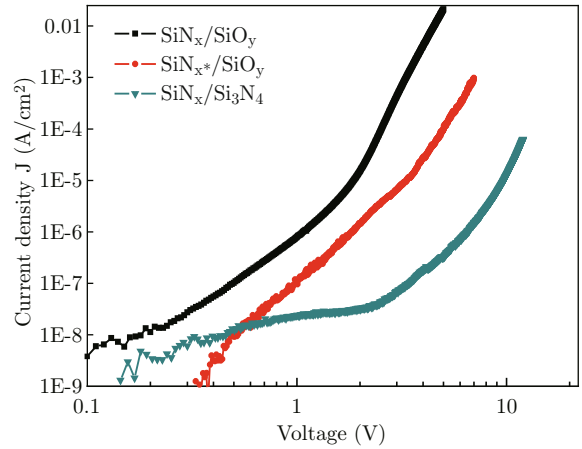


Fig. 4 The J - V curves of annealed $\text{SiN}_x/\text{Si}_3\text{N}_4$, $\text{SiN}_x/\text{SiO}_y$ and $\text{SiN}_{x^*}/\text{SiO}_y$ samples at room temperature.

Temperature dependent I - V was implemented to clarify the transport mechanisms of these samples. The inset of Fig. 5 shows effect of temperature on the J - V characteristics of $\text{SiN}_x/\text{SiO}_y$ sample at high electrical field (applied voltage > 1 V). Due to the temperature dependence of the current, models of tunneling mechanism cannot be used to explain the transport properties of these samples, such as the direct tunneling [23], the Fowler-Nordheim tunneling [24], or the trap-assisted tunneling [25]. But the temperature behavior and voltage dependence indicate that Poole-Frenkel emission, which is based on the emission of trapped electrons towards the dielectric conduction band, can best describe the transport properties. Figure 5 shows the $J/V - V^{1/2}$ plots of all samples at room temperature. The Poole-Frenkel emission is governed by following equation:

$$J_{PF} \propto V \exp \left[- (q/nkT) \left(\varphi_t - \sqrt{qV/d\pi\epsilon} \right) \right]$$

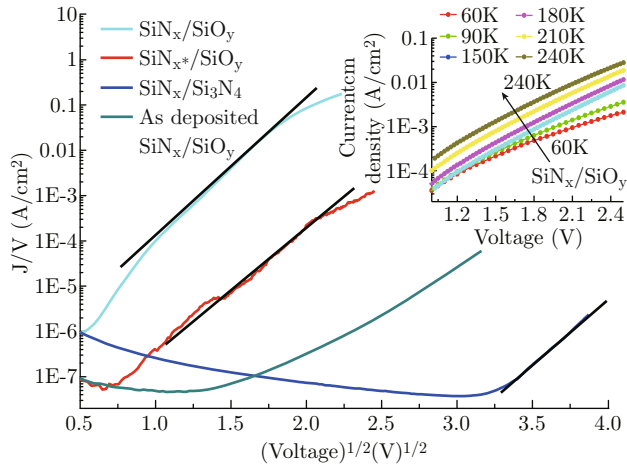


Fig. 5 The Poole-Frenkel plot of annealed $\text{SiN}_x/\text{Si}_3\text{N}_4$, $\text{SiN}_x/\text{SiO}_y$ and $\text{SiN}_x^*/\text{SiO}_y$ samples showing a straight line at high voltage region. The as-deposited $\text{SiN}_x/\text{SiO}_y$ sample do not shows P-F emission properties. The inset illustrate the temperature dependent J - V curves of $\text{SiN}_x/\text{SiO}_y$ structure for the high voltage region ($V > 1$ V).

J_{PF} is the current density, q the electronic charge, d is the oxide and nitride thickness, k the Boltzmann constant, T the absolute temperature, ϕ_t the potential barrier at the trap/dielectric interface (at zero field), and ϵ is the dielectric constants, respectively. The as-deposited $\text{SiN}_x/\text{SiO}_y$ sample does not show a PF emission property. The slope of the plot of $\log(I/V)$ versus $V^{1/2}$, which is called Poole-Frenkel plot, is indicated by linear regression through the data points in Fig. 5. These slopes will yield the dielectric constant of samples under test. However, for these samples, due to the hybrid nature of the Si NCs embedded in Si_3N_4 or SiO_2 dielectric layers, the thickness of total dielectric layers can be hardly determined and this makes it difficult to get the real numerical dielectric constants directly from the slopes. Further work is undergoing to investigate the details of the transport mechanism of the novel structure.

In a silicon tandem solar cell, good charge carrier transport between Si NCs is important for the upper solar cell. The present investigation of the $\text{SiN}_x/\text{SiO}_y$ hybrid system demonstrates that Si NCs of different sizes embedded in isolated layers provides a significantly increase of transport properties. Compared to the conventional $\text{SiN}_x/\text{Si}_3\text{N}_4$ structure, the larger Si NCs in SiO_y layers provide a “pathway” of carrier transportation, as shown in Fig. 6. The present of Si NCs in SiO_y significantly decrease distance between the closest NCs on vertical direction, and increase tunneling ability. Furthermore, SiO_y layer acts as “supplying layer” to provide more Si atoms to SiN_x layer, making Si NCs number in SiN_x increase. With increasing Si NCs number in SiN_x layers, absorption improves, generating more electron-hole pairs; meanwhile, denser Si NCs make the photon-induced carriers find the “pathway”

easier and have higher tunneling probability, improving the carrier extracting ability. That is why $\text{SiN}_x/\text{SiO}_y$ structure has more efficient transport ability compared to $\text{SiN}_x/\text{Si}_3\text{N}_4$ counterpart.

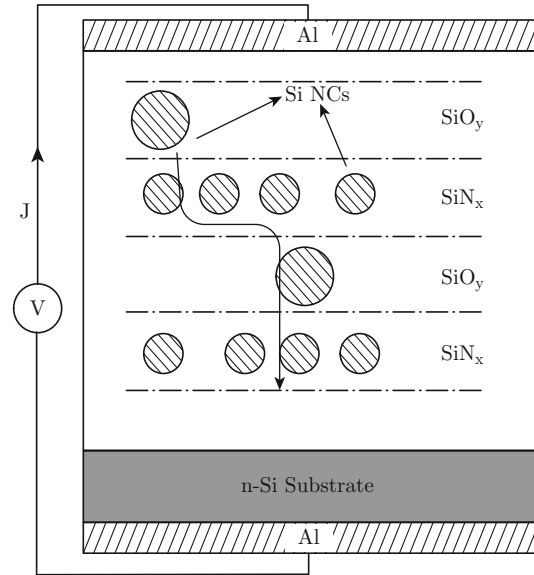


Fig. 6 Schematic transport model of the $\text{SiN}_x/\text{SiO}_y$ system.

Conclusion

The fabrication of Si NCs embedded in a novel $\text{SiN}_x/\text{SiO}_y$ structure using radio frequency magnetron sputtering has been demonstrated. The TEM and Raman spectra clearly indicate that Si NCs appear in each isolated layers, and the presentation of SiO_y layer increase the crystallization volume fraction of SiN_x layers. More Si NCs in this structure obviously enhance the absorption coefficient in ultra-violet region. J - V result indicates that Si NCs in SiO_y layers provide a transport “pathway” for adjacent Si NCs in SiN_x layers. The structures consisting of Si NCs in isolated layers can significantly improve the collection of charge carriers and consequently enhance the efficiency of tandem all-Si solar cells.

Acknowledgments

This work was supported by the National Natural Science Foundation of China (No. 61036001, 51072194 and 60906035)

References

- [1] M. A. Green, “Third Generation photovoltaics”, Springer, Berlin (2003).
- [2] G. Conibeer, M. A. Green, R. Corkish, Y. Cho, E. C. Cho, C. W. Jiang, T. Fangsuwannarak, E. Pink, Y. Huang, T. Puzzer, T. Trupke, B. Richards, A.

- Shalav and K. L. Lin, *Thin Solid Films* 511, 654 (2006). <http://dx.doi.org/10.1016/j.tsf.2005.12.119>
- [3] H. L. Hwang etc, “Handbook of Semiconductor Nanostructures and Nanodevices”, American Scientific Publishers (2006).
- [4] T. Jie, J. W. Shi, L. L. Zhou and Zh. Q. Ma, *Nano-Micro Lett.* 3, 129 (2011). <http://dx.doi.org/10.3786/nml.v3i2.p129-134>
- [5] F. Gourbilleau, C. Ternon, D. Maestre, O. Palais and C. Dufour, *J. Appl. Phys.* 106, 013501 (2009). <http://dx.doi.org/10.1063/1.3156730>
- [6] L. Pavesi, L. D. Negro, C. Moxoloni, G. Franz and F. Priolo, *Nature* 408, 440 (2000). <http://dx.doi.org/10.1038/35044012>
- [7] D. Lu, H. D. Li, S. H. Cheng, J. J. Yuan and X. Y. Lv, *Nano-Micro Lett.* 2, 56 (2010). <http://dx.doi.org/10.5101/nml.v2i1.p56-59>
- [8] D. Pacifici, G. Franz, F. Priolo, F. Iacona and L. D. Negro, *Phys. Rev. B* 67, 245301 (2003). <http://dx.doi.org/10.1103/PhysRevB.67.245301>
- [9] S. Takeoka, M. Fujii and S. Hayashi, *Phys. Rev. B* 62, 16820 (2000). <http://dx.doi.org/10.1103/PhysRevB.62.16820>
- [10] N. M. Park, T. S. Kim and S. J. Park, *Appl. Phys. Lett.* 78, 2575 (2001). <http://dx.doi.org/10.1063/1.1367277>
- [11] J. H. Kim and P. H. Holloway, *J. Appl. Phys.* 95, 4787 (2004). <http://dx.doi.org/10.1063/1.1652226>
- [12] C. W. Jiang and M. A. Green, *J. Appl. Phys.* 99, 114902 (2006). <http://dx.doi.org/10.1063/1.2203394>
- [13] M. A. Green, G. Conibeer, D. König, E. C. Cho, D. Song, Y. Cho, T. Fangsuwannarak, Y. Huang, G. Scardera, E. Pink, S. Huang, C. Jiang, T. Trupke, R. Corkish and T. Puzzer, *Proceedings of the 21st European Photovoltaic Solar Energy Conference*. p10-14 (2006).
- [14] B. Berghoff, S. Suckow, R. Rölver, B. Spangenberg, H. Kurz, A. Sologubenko and J. Mayer, *Sol. Energy Mater. Sol. Cells* 94, 1893 (2010). <http://dx.doi.org/10.1016/j.solmat.2010.06.033>
- [15] M. Marinov and N. Zotov, *Phys. Rev. B* 55, 2938 (1997). <http://dx.doi.org/10.1103/PhysRevB.55.2938>
- [16] G. Faraci, S. Gibilisco, P. Russo, A. R. Pennisi and S. La Rosa, *Phys. Rev. B* 73, 033307 (2006). <http://dx.doi.org/10.1103/PhysRevB.73.033307>
- [17] Ch. Ossadnik, S. Veprek and I. Gregora, *Thin. Solid. Films* 337, 148 (1999). [http://dx.doi.org/10.1016/S0040-6090\(98\)01175-4](http://dx.doi.org/10.1016/S0040-6090(98)01175-4)
- [18] S. Veprek, F.A. Sarott, *Phys. Rev. B* 36, 3344 (1987). <http://dx.doi.org/10.1103/PhysRevB.36.3344>
- [19] J. Zi, H. Buscher, C. Falter, W. Ludwig, K. Zhang and X. Xie, *Appl. Phys. Lett.* 69, 200 (1996). <http://dx.doi.org/10.1063/1.117371>
- [20] E. Bustarret, M. A. Hachicha and M. Brunel, *Appl. Phys. Lett.* 52, 1675 (1988). <http://dx.doi.org/10.1063/1.99054>
- [21] J. Gonzalez-Hernandez and R. Tsu, *Appl. Phys. Lett.* 42, 90 (1983). <http://dx.doi.org/10.1002/pssb.19660150224>
- [22] J. Tauc, R. Grigorovici and A. Vancu, *Phys. Status. Solidi* 15, 627 (1966). <http://dx.doi.org/10.1002/pssb.19660150224>
- [23] S. M. Sze, “Physics of Semiconductor Devices”, Wiley, New York (1981).
- [24] R. H. Fowler and L. Nordheim, *Proc. R. Soc. A* 119, 173 (1928).
- [25] B. Riccò, G. Gozzi and M. Lanzoni, *IEEE Trans. Electron. Devices* 45, 1554 (1998). <http://dx.doi.org/10.1109/16.701488>